nature

SUPPLEMENTARY INFORMATION

https://doi.org/10.1038/s41586-019-1284-2

In the format provided by the authors and unedited.

Selective triplet exciton formation in a single molecule

Kensuke Kimura[1,2], Kuniyuki Miwa[1,3,5], Hiroshi Imada[1]*, Miyabi Imai-Imada[1,2], Shota Kawahara[1], Jun Takeya[2], Maki Kawai[2,4], Michael Galperin[3]* & Yousoo Kim[1]*

[1]Surface and Interface Science Laboratory, RIKEN, Wako, Japan. [2]Department of Advanced Materials Science, Graduate School of Frontier Science, The University of Tokyo, Kashiwa, Japan. [3]Department of Chemistry and Biochemistry, University of California San Diego, La Jolla, CA, USA. [4]Institute for Molecular Science, National Institutes of Natural Sciences, Okazaki, Japan. [5]Present address: Department of Chemistry, Northwestern University, Evanston, IL, USA. *e-mail: himada@riken.jp; migalperin@ucsd.edu; ykim@riken.jp

Supplementary Information

Selective triplet exciton formation in a single molecule

Kensuke Kimura[1, 2], Kuniyuki Miwa[1, 3, 5], Hiroshi Imada[1], Miyabi Imai-Imada[1, 2], Shota Kawahara[1], Jun Takeya[2], Maki Kawai[2, 4], Michael Galperin[3*], and Yousoo Kim[1]**

[1]Surface and Interface Science Laboratory, RIKEN, Wako, Japan.

[2] Department of Advanced Materials Science, Graduate School of Frontier Science, The University of Tokyo, Kashiwa, Japan.

[3] Department of Chemistry & Biochemistry, University of California San Diego, La Jolla 92093, USA.

[4] Institute for Molecular Science, National Institutes of Natural Sciences, Okazaki, Japan.

[5] Present Address: Department of Chemistry Northwestern University, Evanston, IL, USA.

*Correspondence to: himada@riken.jp (H.I.), migalperin@ucsd.edu (M.G.), or ykim@riken.jp (Y.K.).

Here, theoretical analysis for the single molecule electroluminescence within the molecular many-body states description is provided. The supplementary information is organized as follows. In Section A, we introduce model of single molecule junction by defining its Hamiltonian, which accounts for the dynamics of electrons, molecular vibrations, and plasmon. Subsequently, in Section A, we also discuss the calculation technique of tunnelling current and luminescence spectra. Parameters for the first-principles calculations are given in section B. Discussion of computational results and their comparison with experimental data are given in Section C.

A. Electron transport and electroluminescence of a single molecule junction utilizing basis of molecular many-body state

Theoretical analysis for electroluminescence from an isolated PTCDA molecule adsorbed on NaCl(3ML)/Ag(111) is conducted utilizing the basis of the many-body states of the isolated molecule. Since the molecular electronic structure is partially decoupled from the electronic state of metal substrate by the ultrathin insulating film, the intramolecular reorganization upon charging/discharging is expected to be significant and therefore the molecular many-body states are convenient bases for analysing the system properties[44–52]. In the previous studies[46,53], the standard Lindblad/Redfield quantum master equation technique was utilized. This technique is applicable in region of unphysically high temperatures – for the method to be applicable thermal energy should be bigger than the strength of system-bath coupling. In addition, this technique cannot treat the effects of line broadening due to the system-bath coupling and fails to take proper account of system resonances. In order to overcome these limitations, here we apply the Hubbard non-equilibrium Green's function (NEGF) method, which is recently introduced by us[30]. We simulate single molecule junction transport and electroluminescence. The utilized technique accounts for all the intra-system interactions exactly while system-bath coupling is treated within proper diagrammatic perturbation series expansion, and thus it is not restricted to regime of unphysically high thermal energy[30].

Here, we consider electroluminescence from the junction, where a molecule (*M*) is placed between two electrodes (*L* and *R*), which represent the STM tip and substrate. The molecule exchanges electrons and energy with the electrodes. Energy exchange is modelled as the coupling between molecular exciton and interface plasmon localized near the gap between the STM tip and the sample. Both the molecule and plasmons are treated quantum mechanically. Born-Oppenheimer (vibronic) states of the isolated molecule $|S\rangle = |N, a\rangle|v_n^{N,a}\rangle$ are chosen as a basis in the molecular subspace, where *N* represents the number of excess electrons with respect to the neutral PTCDA molecule, *a* indicates a particular state in the charging block. For example, $|+1, D_0\rangle$ indicates the ground electronic state with doublet spin state for the anion (-1 charged state) and $|0, T_1\rangle$ indicates the first excited electronic state with triplet spin state of the neutral molecule. $|v_n^{N,a}\rangle$ denotes the vibrational state for the electronic state $|N, a\rangle$. Electrons in the electrodes, plasmon, and photons in the radiation field are described within the standard second quantization. Hamiltonian of the junction is

$$\hat{H} = \hat{H}_M + \hat{H}_P + \hat{V}_{MP} + \sum_{B=L,R,\mathrm{rad}} \left(\hat{H}_B + \hat{V}_B\right). \tag{1}$$

Here $\hat{H}_M$ is the molecular Hamiltonian

$$\hat{H}_M = \sum_{S\in M} E_S \hat{X}_{SS} \tag{2}$$

$\hat{H}_P$ models plasmonic excitations

$$\hat{H}_P = \hbar\omega_p \hat{a}^\dagger \hat{a} \tag{3}$$

and $\hat{V}_{MP}$ describes the exciton-plasmon coupling

$$\hat{V}_{MP} = \sum_{S_1,S_2\in M} \left(\Delta_{(S_1S_2)} \hat{X}_{S_1S_2}^\dagger \hat{a} + \mathrm{H.c.}\right). \tag{4}$$

The electrodes (L and R) are modelled as reservoirs of free electrons

$$\hat{H}_K = \sum_{\substack{k\in K \\ \sigma}} \varepsilon_{k\sigma} \hat{c}^{\dagger}_{k\sigma} \hat{c}_{k\sigma} \tag{5}$$

and $\hat{H}_{\mathrm{rad}}$ introduces the radiation field

$$\hat{H}_{\mathrm{rad}} = \sum_{\nu} \hbar\omega_{\nu} \hat{b}^{\dagger}_{\nu} \hat{b}_{\nu} \tag{6}$$

$\hat{V}_K$ ($K = L, R$) describes the electron transfer between the molecule and electrode K

$$\hat{V}_K = \sum_{\substack{k\in K \\ \sigma \\ S_1,S_2\in M}} \left(V_{(S_1S_2)k\sigma} \hat{X}^{\dagger}_{S_1S_2} \hat{c}_{k\sigma} + \mathrm{H.c.} \right) \tag{7}$$

$\hat{V}_{\mathrm{rad}}$ describes the coupling of plasmons to the radiation field

$$\hat{V}_{\mathrm{rad}} = \sum_{\nu} \left(W_{\nu} \hat{a}^{\dagger} \hat{b}_{\nu} + \mathrm{H.c.} \right). \tag{8}$$

In eqs. (1)-(8), $\hat{X}_{S_1S_2} = |S_1\rangle\langle S_2|$ denotes the Hubbard (projection) operator which describes transition between molecular many-body states. $\hat{c}^{\dagger}_{k\sigma}$ ($\hat{c}_{k\sigma}$) is creation (annihilation) operator for electron with spin σ in state k of the contacts. $\hat{a}^{\dagger}$ ($\hat{a}$) and $\hat{b}^{\dagger}_{\nu}$ ($\hat{b}_{\nu}$) create (annihilate) interface plasmon and photon in mode ν of the radiation field, respectively. $V_{(S_1S_2)k\sigma}$ is the electron transfer (ET) matrix element from the electrode into the molecule, resulting in a transition between electronic states $|N, a\rangle \rightarrow |N+1, a'\rangle$, and the transition is dressed with the vibrational overlap integral $\langle v^{N+1,a'}_{n'} | v^{N,a}_{n} \rangle$.

Electron flux I_K from the electrode K to the molecule M and photon flux J_{ph} from the system into the radiation field are calculated using the Meir-Wingreen formula[54,55]. Explicit expressions at steady state are

$$I_K = \int_{-\infty}^{\infty} \frac{d\varepsilon}{2\pi\hbar} I_K(\varepsilon) \equiv \int_{-\infty}^{\infty} \frac{d\varepsilon}{2\pi} \frac{e}{\hbar} \mathrm{Tr}_{\mathrm{ET}}[\sigma_K^<(\varepsilon)\mathcal{G}^>(\varepsilon) - \sigma_K^>(\varepsilon)\mathcal{G}^<(\varepsilon)] \quad (9)$$

$$J_{\mathrm{ph}} = \int_{-\infty}^{\infty} \frac{d\varepsilon}{2\pi\hbar} J_{\mathrm{ph}}(\varepsilon) \equiv \int_{-\infty}^{\infty} \frac{d\varepsilon}{2\pi} \frac{1}{\hbar} \sum_{\nu} |W_\nu|^2 [f_\nu^<(\varepsilon)P^>(\varepsilon) - f_\nu^>(\varepsilon)P^<(\varepsilon)]. \quad (10)$$

Here $\mathrm{Tr}_{\mathrm{ET}}[\cdots]$ indicates trace over all electron transfer transition in M. $\sigma_K^<$ and $\sigma_K^>$ are respectively lesser and greater projections of the electron self-energy owing to coupling to the electrode K

$$[\sigma_K(\tau,\tau')]_{(S_1S_2)(S_3S_4)} \equiv \sum_{\substack{k\in K \\ \sigma}} V_{(S_1S_2)k} g_{k\sigma}(\tau,\tau') V_{k(S_3S_4)}. \quad (11)$$

Here $g_{k\sigma}(\tau,\tau') = -\frac{i}{\hbar}\langle T_C \hat{c}_{k\sigma}(\tau)\hat{c}_{k\sigma}^\dagger(\tau')\rangle$ and $f_\nu(\tau,\tau') = -\frac{i}{\hbar}\langle T_C \hat{b}_\nu(\tau)\hat{b}_\nu^\dagger(\tau')\rangle$ are respectively Green's functions for free electron in state k with spin σ of the electrode K and free photon in mode ν of the radiation field. τ and τ' are the Keldysh contour variables, and T_C is the contour ordering operator. $\mathcal{G}^<$ ($\mathcal{G}^>$) in eq. (9) and $P^<$ ($P^>$) in eq. (10) are the lesser (greater) projections of the molecular nonequilibrium Hubbard Green's function and plasmon nonequilibrium Green's function, respectively. $\mathcal{G}$ and P are defined as

$$\mathcal{G}_{(S_1S_2)(S_3S_4)}(\tau,\tau') \equiv -\frac{i}{\hbar}\langle T_C \hat{X}_{S_1S_2}(\tau)\hat{X}_{S_3S_4}^\dagger(\tau')\rangle \quad (12)$$

$$P(\tau,\tau') \equiv -\frac{i}{\hbar}\langle T_C \hat{a}(\tau)\hat{a}^\dagger(\tau')\rangle. \quad (13)$$

Assuming timescale separation between dynamics of electron and vibrational molecular degrees of freedom, we introduce decoupling inherent in the Born-Oppenheimer approximation[56].

$$\mathcal{G}_{(S_1S_2)(S_3S_4)}(\tau,\tau') \approx G_{(N_1a_1N_2a_2)(N_3a_3N_4a_4)}(\tau,\tau') K_{\left(v_1^{N_1a_1}v_2^{N_2a_2}\right)\left(v_3^{N_3a_3}v_4^{N_4a_4}\right)}(\tau,\tau'), \quad (14)$$

where

$$G_{(N_1a_1N_2a_2)(N_3a_3N_4a_4)}(\tau,\tau') \equiv -\frac{i}{\hbar}\langle T_C \hat{X}_{N_1a_1N_2a_2}(\tau)\hat{X}^{\dagger}_{N_3a_3N_4a_4}(\tau')\rangle \tag{15}$$

$$K_{\left(v_1^{N_1a_1}v_2^{N_2a_2}\right)\left(v_3^{N_3a_3}v_4^{N_4a_4}\right)}(\tau,\tau') \equiv \langle T_C \hat{X}_{v_1^{N_1a_1}v_2^{N_2a_2}}(\tau)\hat{X}^{\dagger}_{v_3^{N_3a_3}v_4^{N_4a_4}}(\tau')\rangle. \tag{16}$$

Dressing *K* with vibrational overlap integrals yields generalized Frank-Condon factor

$$FC_{\left(v_1^{N_1a_1}v_2^{N_2a_2}\right)\left(v_3^{N_3a_3}v_4^{N_4a_4}\right)}(\tau,\tau')$$

$$\equiv \left\langle v_1^{N_1a_1}\middle|v_2^{N_2a_2}\right\rangle K_{\left(v_1^{N_1a_1}v_2^{N_2a_2}\right)\left(v_3^{N_3a_3}v_4^{N_4a_4}\right)}(\tau,\tau')\left\langle v_4^{N_4a_4}\middle|v_3^{N_3a_3}\right\rangle. \tag{17}$$

Below we disregard effect of electron dynamics on the Frank-Condon factors FC and assume thermal vibrational distribution. This simplifies Eq. (12) by reducing consideration to diagonal molecular transfers only (i.e. $N_1 = N_3$, $N_2 = N_4$, $a_1 = a_3$, $a_2 = a_4$, $v_1^{N_1a_1} = v_3^{N_3a_3}$, $v_2^{N_2a_2} = v_4^{N_4a_4}$). Evaluation of the electron Green functions G employs second order diagrammatic technique for the Hubbard Green's functions[30]. Plasmon Green function is evaluated within the standard second order diagrammatic perturbation theory[57].

For the problem at hand, main contribution to the signal comes from single electron transfer events. Thus, for simplicity we restrict our consideration to first Hubbard approximation. Following diagrammatic rules formulated in the previous report[30], one gets explicit expressions for the Hubbard self-energy, which consists from contributions of self-energies due to coupling to electrode *K* (*K* = *L*, *R*) and interface plasmon, in the form

$$\Sigma^{K}_{m_1m_2}(\tau_1,\tau_2) = \sum_{m\in \mathrm{ET}} F_{m_1m}[\sigma_K(\tau_1,\tau_2)]_{mm_2} \tag{20}$$

$$\Sigma^{Pl}_{m_1 m_2}(\tau_1, \tau_2)$$

$$= \sum_{b_1 b_2 \in \mathrm{OT}} i\hbar[\sigma_{Pl}(\tau_1, \tau_2)]_{b_1 b_2} N_{\vec{\alpha}(m_1)-\vec{\alpha}(b_1)} s_{\vec{\alpha}(m_1)-\vec{\alpha}(b_1)} g_{l_1 l_2}(\tau_1, \tau_2) N_{\vec{\alpha}(m_2)-\vec{\alpha}(b_2)} s_{\vec{\alpha}(l_2)+\vec{\alpha}(b_2)}$$

$$+ \sum_{b_1 b_2 \in \mathrm{OT}} i\hbar[\sigma_{Pl}(\tau_2, \tau_1)]_{b_2 b_1} N_{\vec{\alpha}(m_1)+\vec{\alpha}(b_1)} s_{\vec{\alpha}(m_1)+\vec{\alpha}(b_1)} g_{l\prime_1 l\prime_2}(\tau_1, \tau_2) N_{\vec{\alpha}(m_2)+\vec{\alpha}(b_2)} s_{\vec{\alpha}(l\prime_2)-\vec{\alpha}(b_2)}. \quad (21)$$

Here m represents electron transition $|N_1, a_1\rangle \rightarrow |N_2, a_2\rangle$ caused by the electron transfer from the electrode to the molecule. $F_{m_1 m_2}(\tau)$ is spectral weight defined as $F_{m_1 m_2}(\tau) \equiv \langle\{\hat{X}_{m_1}(\tau); \hat{X}^{\dagger}_{m_2}(\tau)\}\rangle$.

$$N_{\vec{\alpha}(m)-\vec{\alpha}(b)} s_{\vec{\alpha}(m)-\vec{\alpha}(b)} \hat{X}_l \equiv \left[\hat{X}_m; \hat{X}^{\dagger}_b\right] \quad (22)$$

$$N_{\vec{\alpha}(m)+\vec{\alpha}(b)} s_{\vec{\alpha}(m)+\vec{\alpha}(b)} \hat{X}_{l\prime} \equiv \left[\hat{X}_m; \hat{X}_b\right], \quad (23)$$

where $N_{\vec{\alpha}}$ is equal to 1 when the root vector[58] $\vec{\alpha}$ exists, and 0 otherwise. $s_{\vec{\alpha}(m)-\vec{\alpha}(b)}$ and $s_{\vec{\alpha}(m)+\vec{\alpha}(b)}$ is the sign (± 1) resulting from the commutator $\left[\hat{X}_m; \hat{X}^{\dagger}_b\right]$ and $\left[\hat{X}_m; \hat{X}_b\right]$, respectively. l and l' are defined as $\vec{\alpha}(l) = \vec{\alpha}(m) - \vec{\alpha}(b)$ and $\vec{\alpha}(l') = \vec{\alpha}(m) + \vec{\alpha}(b)$. σ_{Pl} is electron self-energy owing to exciton-plasmon coupling

$$\left[\sigma_{pl}(\tau, \tau')\right]_{(S_1 S_2)(S_3 S_4)} \equiv \sum_K \Delta_{(S_1 S_2)} P(\tau, \tau') \Delta^*_{(S_3 S_4)}. \quad (24)$$

Here P is plasmon nonequilibrium Green's function defined in Eq. (13). P is calculated from the Dyson equation

$$P(\tau, \tau')$$

$$= P^{(0)}(\tau, \tau') + \sum_{S_1, S_2, S_3, S_4 \in M} \iint d\tau_1 d\tau_2 \, P^{(0)}(\tau, \tau_1) \Delta^*_{(S_1 S_2)} \mathcal{g}_{(S_1 S_2)(S_3 S_4)}(\tau_1, \tau_2) \Delta_{(S_3 S_4)} P(\tau_2, \tau'). \quad (25)$$

Here, $P^{(0)}$ is plasmon Green's function in the absence of plasmon-molecular exciton coupling ($\Delta = 0$). Note that the plasmon dissipation owing to the coupling to the radiation field and the plasmon excitation

due to the inelastic tunnelling of the STM system are included in $P^{(0)}$ as shown below in Eq. (26)-(28). Fourier transform of the retarded, lesser, and greater projections of the plasmon Green's function are

$$P^{(0)r}(\varepsilon) = \left[\varepsilon - \hbar\omega_p + i\frac{\gamma_{\mathrm{pl}}}{2}\right]^{-1} \tag{26}$$

$$P^{(0)<}(\omega\varepsilon) = 2iN_{pl}(\varepsilon)\Im P^{(0)r}(\varepsilon) \tag{27}$$

$$P^{(0)<}(\varepsilon) = 2i\left[N_{pl}(\varepsilon) + 1\right]\Im P^{(0)r}(\varepsilon) \tag{28}$$

where $\gamma_{\mathrm{pl}} = 2\pi\sum_v |W_v|^2\delta(\varepsilon - \hbar\omega_v)$ is the dissipation rate of plasmon for $\Delta = 0$ and $N_{pl}(\varepsilon)$ is the occupation probability. At steady-state, $N_{pl}(\varepsilon)$ for plasmon excited by inelastic tunnelling between the STM tip and the substrate is given by[59]

$$N_{pl}(\varepsilon) = \begin{cases} T_{pl}\left(1 - \left|\frac{\varepsilon}{eV}\right|\right), & |\varepsilon| < |eV_s| \\ 0, & \text{otherwise} \end{cases} \tag{29}$$

where T_{pl} is a coefficient related to the current amplitude due to the inelastic tunnelling, e is the elementary charge, and V_s is the sample voltage. Because of mutual inter-dependence (see Eq. (21), (24) and (25)), molecular nonequilibrium Hubbard Green's function $\mathcal{G}$ and plasmon nonequilibrium Green's function P are calculated in a self-consistent manner.

B. Parameter setting

B-1. Energies of many-body states extracted from DFT/TD-DFT calculations

To make out calculation representative of a realistic junction, the information of the molecular electronic and vibrational structure is obtained from first-principles calculations. We use the density functional theory (DFT) and time-dependent DFT (TD-DFT) implemented in the software package Gaussian 16[31]. We consider ground electronic states of -1 charged molecule ($|+1, D_0\rangle$) and the neutral

molecule ($|0, S_0\rangle$), as well as singlet and triplet first excited state of the neutral molecule ($|0, S_1\rangle$ and $|0, T_1\rangle$). The geometry optimization and vibrational analysis are conducted for each electronic state (see Method). The simulations yield total energies $E_{N,a}$ of electronic many-body states $|N, a\rangle$ and vibrational overlap integrals $\left\langle v_{n'}^{N',a'} \middle| v_n^{N,a} \right\rangle$. Results of simulations are presented in Table S1 and Fig. S1.

Table S1 | Total energy E^{total} (summation of the electronic and zero-point vibrational energies) for each electronic state

Electronic state	E^{total} (eV)
$\|+1, D_0\rangle$	-37308.7490
$\|0, S_0\rangle$	-37305.5714
$\|0, S_1\rangle$	-37303.0778
$\|0, T_1\rangle$	-37304.3911

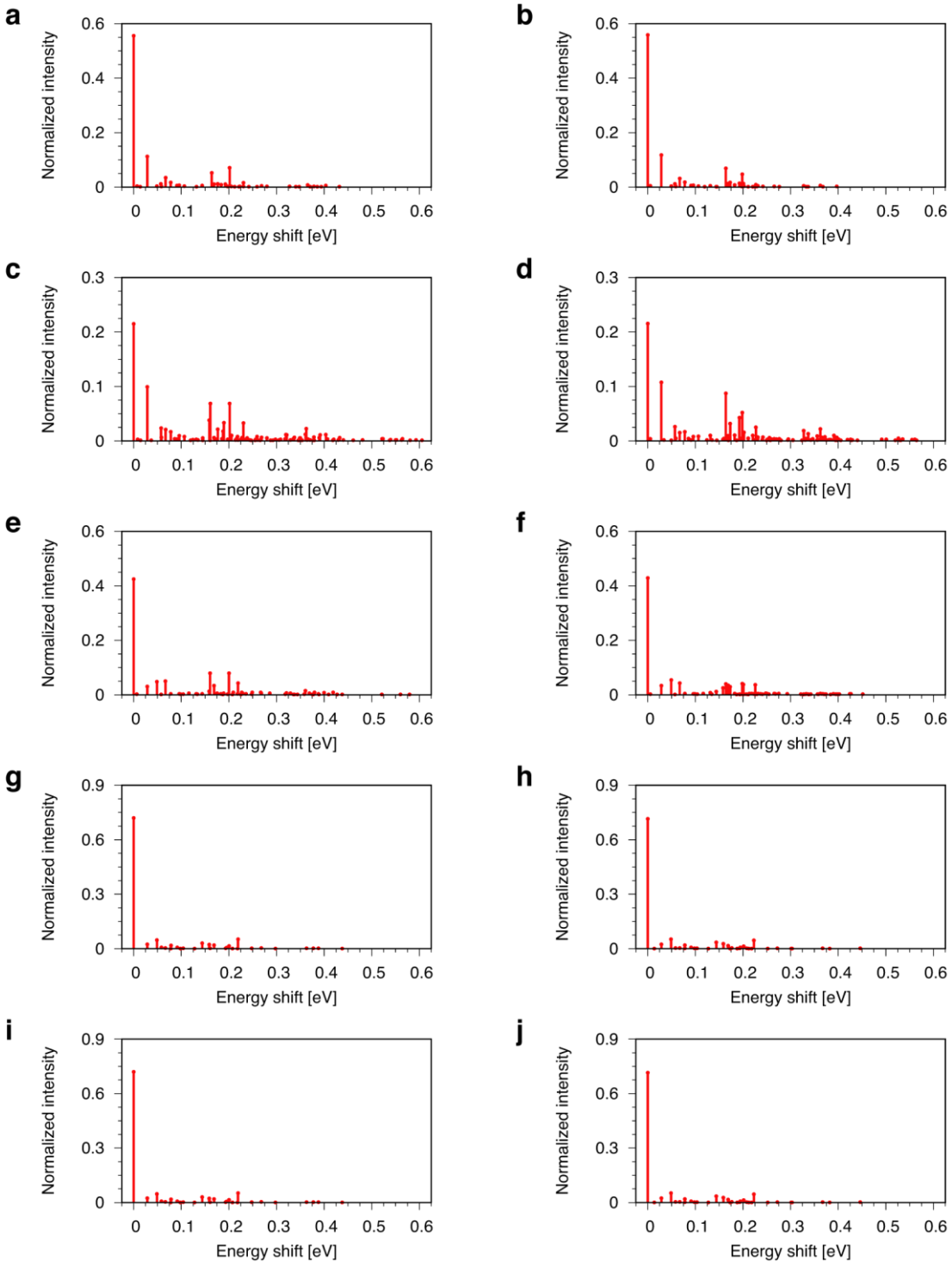

Figure S1 | **Vibrational overlap integral. a-j**, Calculation results for electron transition **a**: $|0, S_0\rangle \rightarrow |0, S_1\rangle$, **b**: $|0, S_1\rangle \rightarrow |0, S_0\rangle$, **c**: $|0, S_0\rangle \rightarrow |0, T_1\rangle$, **d**: $|0, T_1\rangle \rightarrow |0, S_0\rangle$, **e**: $|0, S_0\rangle \rightarrow |+1, D_0\rangle$, **f**: $|+1, D_0\rangle \rightarrow |0, S_0\rangle$, **g**: $|0, S_1\rangle \rightarrow |+1, D_0\rangle$, **h**: $|+1, D_0\rangle \rightarrow |0, S_1\rangle$, **i**: $|0, T_1\rangle \rightarrow |+1, D_0\rangle$, **j**: $|+1, D_0\rangle \rightarrow |0, T_1\rangle$,

B-2. Effects of image interaction with the metal substrate on the energy for molecule many-body state transitions

Here we discuss image interaction energy for PTCDA molecule adsorbed on a NaCl ultrathin film grown on a metal surface. The energy for electron/hole attachment to the molecule adsorbed on ultrathin insulating film grown on the metal substrate is significantly different from the one for the molecule in the gas phase, because the molecule is situated near the metal substrate (~ 1 nm)[45,60]. In the previous report[60], it was proved that the differences are mainly attributed to the image interaction with the metal substrate. Here, the effects of image interaction are evaluated with the aid of the dielectric model proposed in the report[60]. In this model, the insulating film is treated as a homogeneous dielectric material, and the metal as a perfect conductor. The charged molecule is treated as a homogeneously charged rectangular sheet with a net charge of $\pm e$, where e is the elementally charge. Following the report[60], the values for the side lengths of rectangular sheet, $D_x = 11.43$ Å$, D_y = 6.68$ Å, are determined from the size of molecular structure (here, the optimized geometry of PTCDA molecule for ground electronic state). We employ parameters determined from the DFT calculations for NaCl(3ML) film adsorbed on the metal substrate as was given in the report[60]. Resulting shift for the electron/hole attachment energies is estimated as 0.862 eV. In the following discussion, effects of the image interaction on the electron/hole attachment energies are included in the evaluation of the transition energies.

B-3. Parameters for electrostatic-potential drops in NaCl film and the tip-sample vacuum region, plasmon resonance, and electron escape rates

Other necessary parameters were chosen to be representative of a realistic experimental situation as follows, based on previous studies. The drop of electrostatic potential in both NaCl film and the vacuum region between the STM tip and the sample is evaluated taking the dielectric constant of NaCl film as 5.62[47,61], the effective thickness of the NaCl film as 921 pm[60], the vacuum region as 1.0 nm, and the work function of NaCl(3ML)/Ag(111) as 3.57 eV[39]. Following the previous report[53], the dissipation rate for the plasmon is set as $\gamma_{\mathrm{pl}} = 210$ meV. As used in the previous reports[17,18], the value of coefficient T_{pl} related to the current amplitude owing to the inelastic tunnelling is set as $T_{pl} = 10^{-4}$. The coupling of plasmon to the molecular exciton related to the $S_0 - S_1$ transition is set as $\Delta_{(0,S_0;0,S_1)} = 20$ meV[62] and that of the $S_0 - T_1$ transition is set as $\Delta_{(0,S_0;0,T_1)} = 10$ meV, considering the rate of singlet-triplet transition of 10^3 s^{-1} in the literature[62] and enhancement of electric field by plasmon resonance of ~$10^{4\text{-}6}$.

Based on the previous reports[28,60], the electron escape rate to the metal substrate $\gamma_R = 2\pi \sum_{k\in R} |V_{\eta k}|^2 \delta(\varepsilon - \varepsilon_k)$ is set as $\gamma_R = 0.400$ meV. The electron escape rate to the STM tip $\gamma_L = 2\pi \sum_{k\in L} |V_{\eta k}|^2 \delta(\varepsilon - \varepsilon_k)$ is set as γ_L =0.001 meV. These values yield tunnelling current in the sub-nano amperes region, which agree with the experiment. It is noteworthy that the measured $\mathrm{d}I_t/\mathrm{d}V_s$ spectra display broad peaks with width of ~300 meV (Fig. 1c, 3d), on the other hand the measured luminescence spectral show sharp peak (Fig. 2e). Considering the experimental situation where the molecular electronic structure is decoupled from metal electronic states by the ultrathin insulating film, the electron escape rate is very low[28,59]. According to the previous reports[28,63–66], the broad peak widths observed in $\mathrm{d}I_t/\mathrm{d}V_s$ spectra are attributed to the coupling between electron and substrate phonon. In particular, it was reported that strong electron-phonon coupling causes broad line profiles observed for a localized electronic state caused by chlorine vacancies in ultrathin NaCl film grown on a metal substrate[28]. Moreover, the variation of the peak width in the $\mathrm{d}I_t/\mathrm{d}V_s$ spectra was observed for a molecule on various types of insulating films, such as

NaCl, RbI, and Xe films[64,65]. Therefore, it is expected that the electron–phonon coupling makes the dominant contribution to the peak width observed in the dI_t/dV_s spectra. However, the electron-phonon coupling does not affect significantly the onset voltages in the dI_t/dV_s spectrum and the threshold voltages for S_1 and T_1 formation. Because the threshold voltage for exciton formation is main interest here and for the sake of simplicity, the analysis proceeds without taking the electron-phonon coupling into account.

C. Simulation results of single molecule luminescence spectra

The theoretical method based on Hubbard NEGF technique was applied to simulate the STL spectrum. A calculated STL spectrum at V_s = -3.6 V is shown in Fig. S2. A broad peak and several sharp peaks appear in the spectrum. The broad peak at 2.5 eV is attributed to the radiative decay of the plasmon. According to the theoretical analysis on the many-body states transition, the peak at 1.18 eV is attributed to the $|0, T_1\rangle \rightarrow |0, S_0\rangle$ transition (phosphorescence), and the low-intensity peaks in the energy range of 1.00 – 1.18 eV are attributed to the $|0, T_1\rangle \rightarrow |0, S_0\rangle$ transitions associated with the vibrational transitions. Similarly, the peaks at 2.49 eV is attributed to the $|0, S_1\rangle \rightarrow |0, S_0\rangle$ transition (fluorescence), and the low-intensity peaks in the energy range of 2.30– 2.49 eV are the vibrational satellites. The results are in good agreement with the experimental results shown in Fig. 2 of the main text.

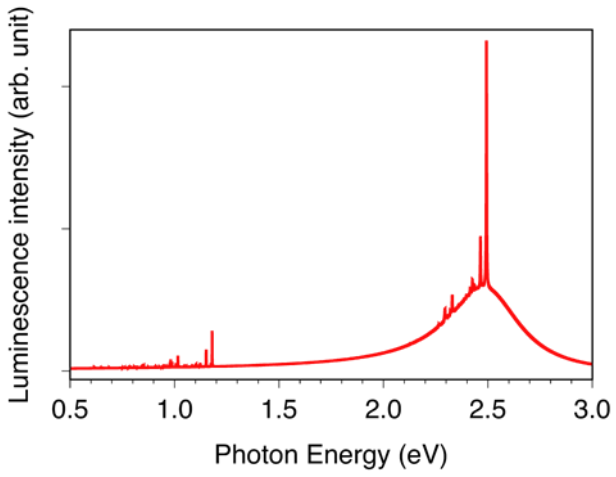

Figure S2 | **A simulation result for STL spectrum of PTCDA/NaCl/Ag(111).** The sample voltage (V_s) is set as -3.6 V and the energy of plasmon mode $\hbar\omega_p$ is set as 2.5 eV.

Next, we simulated the plasmon enhancement effect on the phosphorescence and fluorescence. The STL spectra at V_s = -3.6 V are calculated with changing the energy of the plasmon mode $\hbar\omega_p$ from 1.5 eV to 2.9 eV, and the (Fig. S3). As changing $\hbar\omega_p$, the intensity ratio between the fluorescence (2.49 eV) and phosphorescence (1.18 eV) changes, which reproduces the experimental result shown in Extended Data Fig. 5.

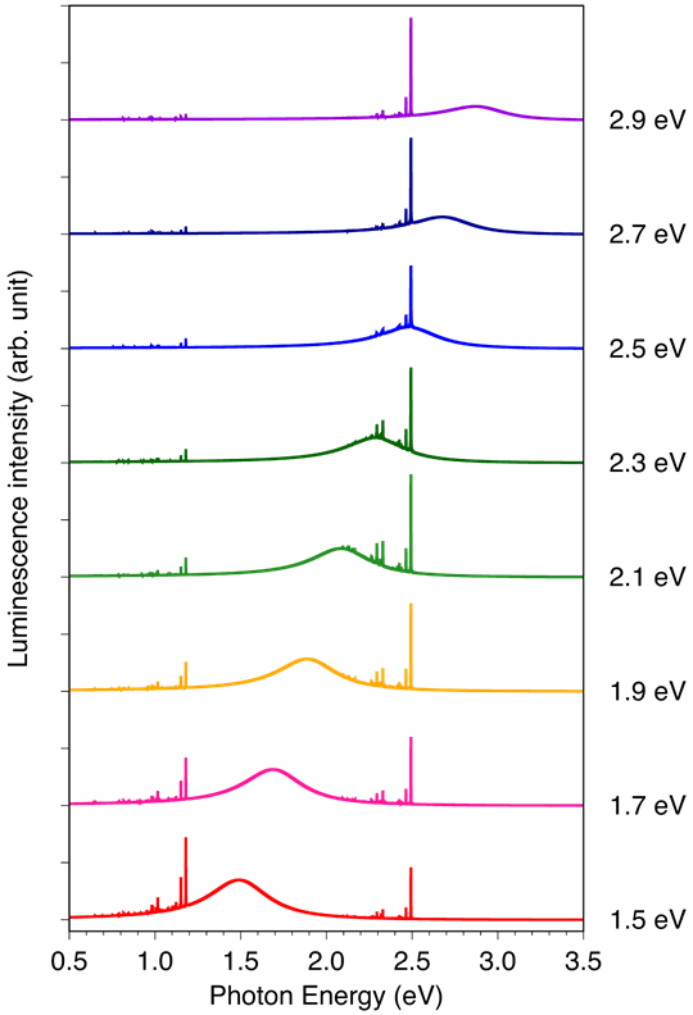

Figure S3 | **Simulation results for the dependence of STL spectra on the energy of the plasmon mode.** The energy of the plasmon mode $\hbar\omega_p$ is changed from 1.5 eV to 2.9 eV by 0.2 eV. The sample voltage is set as V_s = -3.6 V in the all calculations.

For revealing the exciton formation mechanism, we calculated the sample voltage dependence of luminescence spectra. Figure S4a and S4b show a series of phosphorescence and fluorescence spectra calculated at different sample voltages. The energy of plasmon mode $\hbar\omega_p$ is set as 2.5 eV in the simulations here. As the sample voltage is decreased, the phosphorescence appears at V_s = -2.0 V, and the fluorescence appears at V_s = -3.5 V, which are well reproducing the sample voltage dependence in Fig. 3a and 3b. The photon intensities of phosphorescence and fluorescence are plotted as a function of the sample voltage in Fig. S4c, which clearly shows that the threshold voltage for phosphorescence (V_{th}^{p}) and fluorescence (V_{th}^{f}) are -1.92 V and -3.46 V in the simulation. The width of peak at 2.49 eV in Fig. S4b is wider than that of at 1.18 eV in Fig. S4a. The difference between the peak widths in the simulation can be explained by the following two factors. Fist, the exciton-plasmon coupling $\Delta_{(0,S_0;0,S_1)}$ is stronger than $\Delta_{(0,S_0;0,T_1)}$. Second, the energy of plasmon mode $\hbar\omega_p$ is close to the energy of the $|0,S_1\rangle \rightarrow |0,S_0\rangle$ transition. The $|0,S_1\rangle \rightarrow |0,S_0\rangle$ transition is promoted owing to the coupling with the plasmon, leading to the shorted lifetime of the $|0,S_1\rangle$ state and the wider peak in the luminescence spectra in this simulation.

Figure S4d shows the calculated dI_t/dV_s spectrum. According to the calculation results for the probability of each many-body states at various sample voltages, the sharp peak at V_s = -0.55 eV is originated from the many-body transition of $|+1,D_0\rangle \rightarrow |0,S_0\rangle$, -1.92 V is the transition of $|+1,D_0\rangle \rightarrow |0,T_1\rangle$, and -3.46 V is the transition of $|+1,D_0\rangle \rightarrow |0,S_1\rangle$. The calculated spectrum successfully reproduces the peak positions observed in the experimental dI_t/dV_s spectrum (Fig. 3d). The low intensity peaks around the strong peaks are the many-body state transition associated with vibrational excitations. The gradual increase in the dI_t/dV_s spectrum is observed at V_s < -1.5 V in the experimental results (Fig. 3d and 4b), which is caused by the tunnelling from Ag(111) substrate. The gradual increase is not reproduced in the theoretical calculation, because the electrodes (tip and substrate) are modelled within the wide band approximation which misses realistic structure of its spectral function (Section A).

Comparing to Fig. S4c and S4d, the threshold voltages for V_{th}^{p} and V_{th}^{f} are corresponding to the position of the peaks in dI_t/dV_s spectrum. The results indicate that the extraction of the electron from the molecule triggers the formation of exciton in the molecule, which strongly support our interpretation of the selective T_1 formation mechanism.

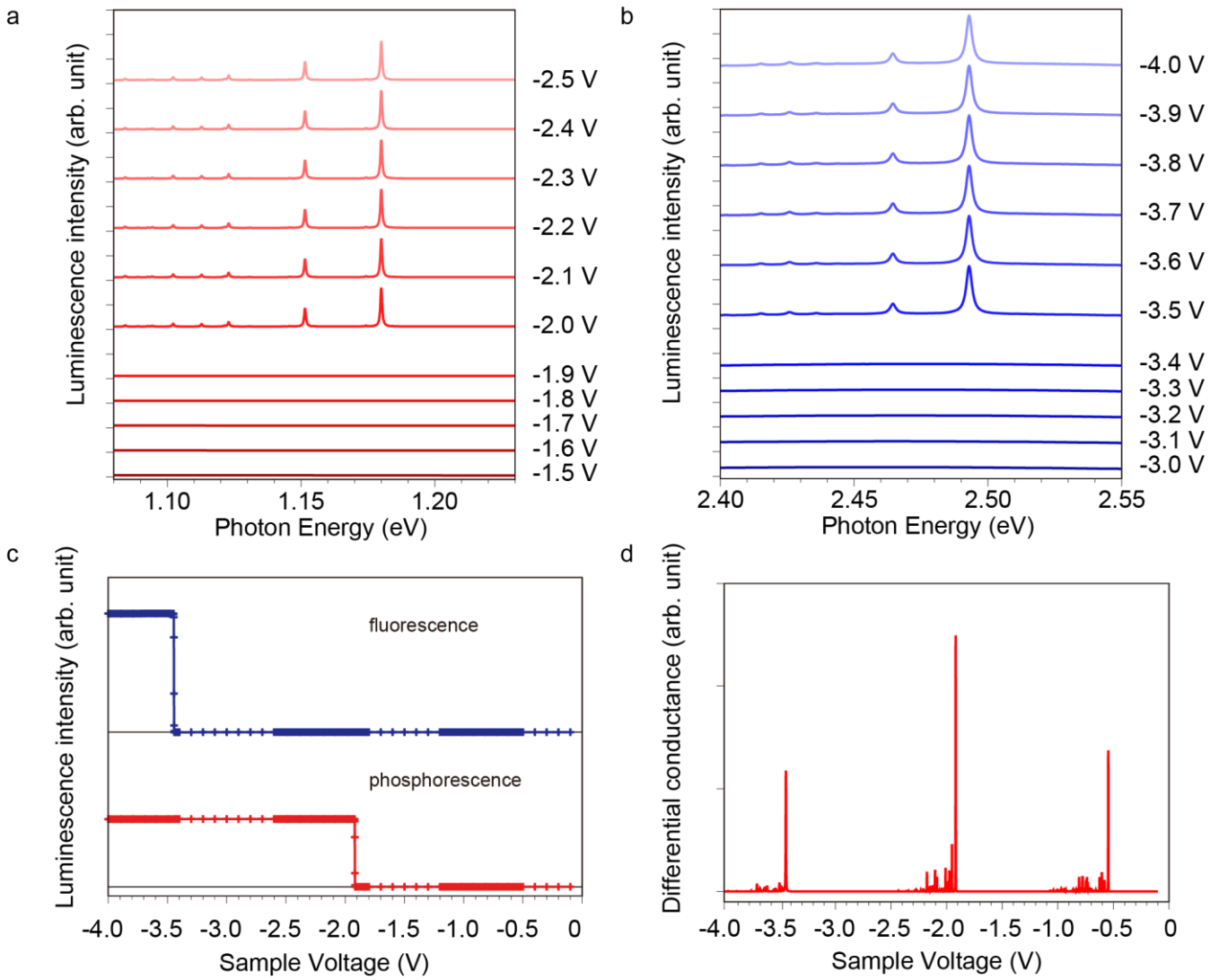

Figure S4 | **Simulation results for the sample voltage dependence of STL spectra, luminescence intensity and the dI_t/dV_s spectrum. a-b**, Series of luminescence spectra ($\hbar\omega_p = 2.5$ eV). **a**: Phosphorescence (V_s = -1.5 – -2.5 V). **b**: Fluorescence (V_s = -3.0 – -4.0 V). **c**. Sample voltage dependence of luminescence intensities at the energy of fluorescence (2.49 eV) and phosphorescence (1.18 eV) for $\hbar\omega_p$ = 2.5 eV. The STL spectra are calculated at V_s = -0.1 V – -4.0 V. STL spectra were calculated by V_s = 0.001 V in the regions of -4.0 < V_s < -3.4 V, -2.5 < V_s < -1.8 V, and -1.1 < V_s < -0.5 V. Other regions were calculated by V_s = 0.1 V. **d**: a simulation result for dI_t/dV_s spectrum

References for Supplemental Information

44. Schulz, F. *et al.* Many-body transitions in a single molecule visualized by scanning tunnelling microscopy. *Nat. Phys.* **11**, 229–234 (2015).

45. Ervasti, M. M., Schulz, F., Liljeroth, P. & Harju, A. Single- and many-particle description of scanning tunneling spectroscopy. *J. Electron Spectrosc. Relat. Phenom.* **219**, 63–71 (2017).

46. Seldenthuis, J. S., van der Zant, H. S. J., Ratner, M. A. & Thijssen, J. M. Electroluminescence spectra in weakly coupled single-molecule junctions. *Phys. Rev. B* **81**, 205430 (2010).

47. Fatayer, S. *et al.* Reorganization energy upon charging a single molecule on an insulator measured by atomic force microscopy. *Nat. Nanotechnol.* **13**, 376–380 (2018).

48. Yu, P., Kocić, N., Repp, J., Siegert, B. & Donarini, A. Apparent Reversal of Molecular Orbitals Reveals Entanglement. *Phys. Rev. Lett.* **119**, 056801 (2017).

49. White, A. J., Ochoa, M. A. & Galperin, M. Nonequilibrium Atomic Limit for Transport and Optical Response of Molecular Junctions. *J. Phys. Chem. C* **118**, 11159–11173 (2014).

50. White, A. J., Fainberg, B. D. & Galperin, M. Collective Plasmon-Molecule Excitations in Nanojunctions: Quantum Consideration. *J. Phys. Chem. Lett.* **3**, 2738–2743 (2012).

51. Galperin, M. Photonics and spectroscopy in nanojunctions: a theoretical insight. *Chem. Soc. Rev.* **46**, 4000–4019 (2017).

52. Miwa, K., Chen, F. & Galperin, M. Towards Noise Simulation in Interacting Nonequilibrium Systems Strongly Coupled to Baths. *Sci. Rep.* **7**, 9735 (2017).

53. Tian, G. & Luo, Y. Electroluminescence of molecules in a scanning tunneling microscope: Role of tunneling electrons and surface plasmons. *Phys. Rev. B* **84**, 205419 (2011).

54. Haug, H. & Jauho, A.-P. Quantum Kinetics in Transport and Optics of Semiconductors, 2nd ed.; Springer, 2008; p 362.

55. Gao, Y. & Galperin, M. Optical spectroscopy of molecular junctions: Nonequilibrium Green's functions perspective. *J. Chem. Phys.* **144**, 174113 (2016).

56. Galperin, M., Nitzan, A. & Ratner, M. A. Resonant inelastic tunneling in molecular junctions. *Phys. Rev. B* **73**, 045314 (2006).

57. Mahan, G. D. Many-Particle Physics, 3rd ed. Plenum, New York, 2000, p.785.

58. Ovchinnikov, S. G. & Val'kov, V. V. Systems Operators in the Theory of Strongly Correlated Electrons; Imperial College Press, 2004.

59. Persson, B. N. J. & Baratoff, A. Theory of photon emission in electron tunneling to metallic particles. *Phys. Rev. Lett.* **68**, 3224–3227 (1992).

60. Scivetti, I. & Persson, M. Frontier molecular orbitals of a single molecule adsorbed on thin insulating films supported by a metal substrate: electron and hole attachment energies. *J. Phys. Condens. Matter* **29**, 355002 (2017).

61. A.J. Dekker. Solid State Physics, Prentice-Hall, Englewood Cliffs, 1957.

62. Manjavacas, A., García de Abajo, F. J. & Nordlander, P. Quantum Plexcitonics: Strongly Interacting Plasmons and Excitons. *Nano Lett.* **11**, 2318–2323 (2011).

63. Repp, J., Meyer, G., Stojković, S. M., Gourdon, A. & Joachim, C. Molecules on Insulating Films: Scanning-Tunneling Microscopy Imaging of Individual Molecular Orbitals. *Phys. Rev. Lett.* **94**, 026803 (2005).

64. Liljeroth, P., Repp, J. & Meyer, G. Current-Induced Hydrogen Tautomerization and Conductance Switching of Naphthalocyanine Molecules. *Science* **317**, 1203–1206 (2007).

65. Pavliček, N., Swart, I., Niedenführ, J., Meyer, G. & Repp, J. Symmetry Dependence of Vibration-Assisted Tunneling. *Phys. Rev. Lett.* **110**, 136101 (2013).

66. Jdira, L. *et al*. Linewidth of resonances in scanning tunneling spectroscopy. *Phys. Rev. B* **77**, (2008).